



Multi-temporal hyperspectral mixture analysis and feature selection for invasive species mapping in rainforests



Ben Somers ^{a,*}, Gregory P. Asner ^b

^a Flemish Institute for Technological Research (VITO), Centre for Remote Sensing and Earth Observation Processes (TAP), Boeretang 200, BE-2400 Mol, Belgium

^b Carnegie Institution for Science, Department of Global Ecology, 260 Panama Street, Stanford, CA 94305 USA

ARTICLE INFO

Article history:

Received 5 November 2012

Received in revised form 10 April 2013

Accepted 14 April 2013

Available online 20 May 2013

Keywords:

MESMA

Stable Zone Unmixing

Hyperion

Time series analysis

Unmixing

Spectroscopy

Morella faya

Phenology

Hawaii

ABSTRACT

We evaluated the potential of a multi-temporal Multiple Endmember Spectral Mixture Analysis (MESMA) for invasive species mapping in Hawaiian rainforests. Earth Observing-1 Hyperion time series data were compiled in a single image cube and ingested into MESMA. While the temporal analysis provided a way to incorporate species phenology, a feature selection technique automatically identified the best time and best spectral feature set to optimize the separability among the native and invasive tree species in our study area. We initiated an alternative Separability Index (SI)-based feature selection approach in which a boundary condition reduced the amount of correlation in the selected spectral subset. We hypothesized that redundant spectral information could be avoided, and improved plant detection accuracy could be achieved, with reduced computational time due to the selection of fewer bands in the mixture analysis. Our analysis showed a systematic increase in the invasive species detection success when we compared the output of multi-temporal MESMA ($Kappa = 0.78$) with that of the traditional unitemporal approach ($Kappa = 0.51–0.69$). Even for unitemporal MESMA, in which only a single input image was used, the band selection strategy was beneficial both in plant detection accuracy and computational time. We could further demonstrate that, despite a lack of imagery covering all phenological events, a proper band selection strategy can emphasize subtle spectral and phenological differences between species and can thereby partly compensate for this lack of data. This creates opportunities for mapping in areas where cloud cover is a limiting factor for building extended spectral image time series. This approach is sufficiently general and inherently adaptive, thereby supporting species mapping using Hyperion and forthcoming space-borne imaging spectrometers.

© 2013 Elsevier Inc. All rights reserved.

1. Introduction

The rapid spread of non-native invasive plant species is currently considered one of the most significant threats to global biodiversity and ecosystem functioning (Vitousek et al., 1997). Remote detection, mapping and monitoring of biological invasion are critical components of conservation and management efforts, but the high spectral similarity between plant species often complicates spectral image interpretation (Zhang et al., 2006). Recent developments in hyperspectral remote sensing offer potential advantages. As opposed to traditional multi-spectral sensors, hyperspectral sensors provide detailed spectra allowing a better discrimination between plant species (Clark et al., 2005). Airborne hyperspectral sensors have demonstrated potential for invasive species mapping (e.g., Glenn et al., 2005; Hestir et al., 2008; Lawrence et al., 2006; Parker & Hunt, 2004; Underwood et al., 2003) but the relatively high cost of aerial surveys and the consequent lack of year-round monitoring are known limitations for setting up a

continuous monitoring program over large areas (review by He et al., 2011).

Spaceborne hyperspectral sensors, such as the Earth Observing-1 Hyperion, the upcoming Environmental Mapping and Analysis Program (EnMap), Hyperspectral Infrared Imager (HyspIRI) and Precursore Iperspettrale della Missione Applicativa (Prisma) missions, might provide a powerful alternative. Spaceborne imaging spectroscopy provides spectral detail, systematic revisits and global coverage, but inevitably comes with a decreased spatial detail. Hyperion's ground sampling distance of 30 m consequently results in image pixels composed of mixtures of different ground components (e.g. invasive species, native species, soil, shadow), potentially limiting the ability for invasive species detection (Huang & Asner, 2009). Multiple Endmember Spectral Mixture Analysis (MESMA), a common technique providing sub-pixel cover distribution maps, is generally used to address this mixture problem (Roberts et al., 1998). Its accuracy remains moderate, however, when dealing with mixtures composed of highly similar vegetation endmembers (review by Somers et al., 2011).

Hyperion's ability to systematically revisit targeted areas, opens new perspectives to reduce these spectral similarity issues. By combining spectral information from different periods of the growing

* Corresponding author. Tel.: +32 14336768.

E-mail address: ben.somers@vito.be (B. Somers).

season, phenological differences between plant species can be captured, consequently improving overall detection and mapping accuracy. Although this hypothesis is well acknowledged, the number of studies evaluating seasonal spectral separability among plant species is limited. The effects of vegetation phenology on species mapping in the Californian chaparral were studied by [Dennison and Roberts \(2003\)](#). More recently, [Hesketh and Sanchez-Azofeifa \(2012\)](#) evaluated the seasonal leaf-level spectral separability in the dry forests of Panama. In our previous work, we clearly demonstrated the benefits of integrating Hyperion time series data in MESMA for invasive species mapping in the Hawaiian rainforests ([Somers & Asner, in press](#)). We observed a significant increase in invasive species detection success when spectral information from different moments in the growing season was integrated into MESMA. We developed a multi-step method that resulted in a composite image built from the four spectral regions (visible (VIS), near-infrared-1 (NIR1), NIR2, and short-wave infrared (SWIR)), each taken from different months. Although we could clearly demonstrate the benefit of such a multi-temporal hyperspectral unmixing approach for invasive species detection, the simple image stacking approach is not optimal because:

- (1) It does not allow us to address or highlight subtle phenological events that often only express themselves as spectral differences among narrow wavebands, rather than by changing the reflectance of all bands in one of the four broad spectral regions (e.g. changes in chlorophyll a pigmentation will only result in notable changes in a small waveband zone around the 680 nm absorption peak; [Richardson et al., 2002](#)). Some of these subtle but possibly important phenological events and spectral differences will, as such, be masked or missed in our simplified image stacking approach since, for each broad spectral region, the spectral information is extracted from the same image or from the same month.
- (2) The stacking approach does not allow us to include spectral information from the same spectral bands but from a different moment in the growing season. Each band could only be used once. Again this means that we are not able to incorporate phenology fully because it is possible that two independent phenological events (e.g. one in winter, the other one in summer) both affect the same spectral region. Optimal spectral separability between the species would thus require the same band from two seasons to be incorporated into MESMA.

We hypothesize that to fully exploit the differences in plant phenology and optimize spectral separability between the native and invasive species, we need to integrate multi-temporal unmixing and automated feature extraction. [Asner and Lobell \(2000\)](#) were the first to highlight the benefits of feature selection in spectral mixture analysis. Previous studies had already revealed that the SWIR2 spectral information (2000–2500 nm) is useful to separate leaf, litter and soil material ([Asner et al., 2000](#); [Daughtry, 2001](#); [Roberts et al., 1993](#)). [Asner and Lobell \(2000\)](#), therefore only used SWIR2 information in their iterative and automated spectral unmixing algorithm called AutoSWIR. Although successfully tested in several ecosystems, the applicability of AutoSWIR requires high-fidelity SWIR2 measurements, which are not currently available from Earth-orbiting imaging spectrometers. [Somers et al. \(2010\)](#) presented an alternative, more flexible band selection approach for unmixing, referred to as Stable Zone Unmixing (SZU). The wavelength sensitivity towards spectral variability is assessed prior to unmixing using the Stability Index (SI), defined as the ratio of the inter-class to the intra-class endmember variability. As opposed to AutoSWIR, SZU has the advantage of automatically adapting the selected spectral subset to each specific scenario, i.e. the sensor performance, the spectral heterogeneity of the image scene and the spectral separability among the presented endmembers or land cover classes. Although successfully tested on in situ measured

hyperspectral data, the performance of the SZU on actual hyperspectral images has not yet been evaluated.

Although not accounted for in AutoSWIR and SZU, we acknowledge that adjacent wavebands in hyperspectral imagery are often highly correlated ([Delalieux et al., 2007](#)). Potential additional gains in detection accuracy as well as in the computational/running time are, however, expected when only decorrelated spectral information is considered in the mixture analysis. Although statistical feature selection methods based on Principal Components Analysis (PCA; [Miao et al., 2006](#)) and Discrete Cosine Transform (DCT; [Li, 2004](#)) can significantly reduce the dimensionality of spectral data, they do not systematically improve abundance estimations ([Li, 2004](#)). These statistical band selection techniques select decorrelated spectral features that explain most of the observed spectral variation in the image. Yet, these spectral subsets do not necessarily optimize the spectral separability between the present endmembers (e.g., natives vs invasives) as is the case for the SI-based band selection in SZU. We therefore propose an alternative SI-based selection protocol in which an additional boundary condition reduces the amount of correlation in the selected spectral subset. It is anticipated that such an approach should improve the accuracy of SZU and other spectral unmixing approaches.

The main objective of this study was to evaluate the potential of combining a time series of hyperspectral images and an automated feature selection technique in MESMA for species detection and mapping in rainforests. While the temporal analysis provides a way to incorporate vegetation phenology, the feature selection technique automatically identifies the best time and best spectral feature set to optimize the separability among the endmembers, potentially boosting the accuracy of plant species detection. A modified SI-based feature selection approach in which a boundary condition is set that forces the selection of decorrelated wavebands is tested on a time series of six Hyperion images covering a Hawaiian rainforest area. The ultimate goal is to improve the detection of invasive tree species in this complex rainforest ecosystem, as a model approach for use in any forested region.

2. Materials and methods

2.1. Study area & species phenology

Our study was conducted in a 300 ha montane rainforest area (19° 24' 00" N, 115° 14' 50" W) in the Hawaii Volcanoes National Park (HAVO) on the Island of Hawaii ([Fig. 1](#)). The HAVO area is located at approximately 1200 m above sea level and is characterized by a mean annual rainfall of 2500 mm ([Giambelluca et al., 1986](#)). Daily average temperatures vary between 14 °C in winter and 17 °C in summer ([Armstrong, 1983](#)). The native Hawaiian forests in our study area were once entirely dominated by the *Metrosideros polymorpha* tree species with an understory mostly comprised of ferns *Cibotium glaucum* and *Dicranopteris linearis* ([Vitousek et al., 1987](#)). However, in the last 50–60 years, these native forests have progressively been invaded by the nitrogen (N) fixing tree *Morella faya*, introduced from the Azores into Hawaii about fifty years ago ([Vitousek et al., 1987](#)). By enriching the N content of the otherwise low fertility soils, while shading out nearly all other species, *M. faya* is drastically altering the nutrient balance and structure of the native *Metrosideros* forests ([Hall & Asner, 2007](#)), and is seen as one of the main threats to native biodiversity ([Vitousek & Walker, 1989](#)).

Ground-based measurements ([Asner et al., 2008b](#)) show that the *Metrosideros* trees in this area are approximately 20 m tall and have a leaf area index (LAI) of about 3. With a LAI > 5 the *Morella* trees have a competitive advantage over the native vegetation ([Vitousek & Walker, 1989](#)). In summer the difference in LAI between both species is even more pronounced due to intensive leaf flushing in *Morella*. The *Morella* trees exploit the favorable summer conditions with moderate rainfall and high photosynthetic active radiation to expand their canopy ([Whiteaker & Gardner, 1992](#)). By contrast, *Metrosideros* is a slow-growing



Fig. 1. (Left) overview of the Hawaii Volcanoes National Park on the Island of Hawaii (imagery from the Carnegie Airborne Observatory; Asner et al., 2008a); (right) detail of the native ohia (*Metrosideros*) forests. Although most of this area is under protection by the U.S. National Park Service, it has experienced a number of biological invasions predominantly by *Morella faya* (from Somers & Asner, in press). The black box indicates the area covered by the Hyperion images.

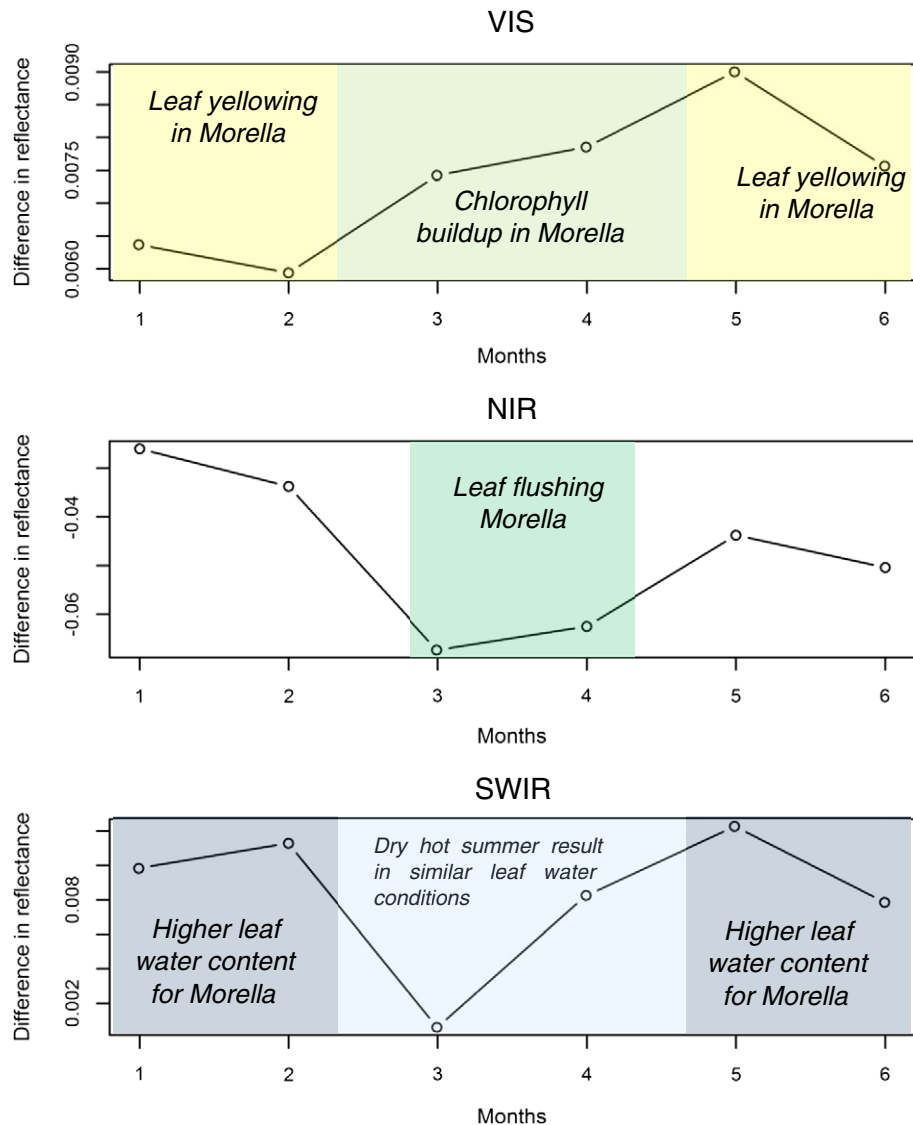


Fig. 2. Illustration of the linkage between ground phenology and the mean difference in Hyperion reflectance between *Metrosideros* and *Morella*. Results are shown for: VIS (400–700 nm), NIR (800–1300 nm), and SWIR (1500–1700 nm) reflectance (supported by Asner et al., 2006; Somers & Asner, in press, 2012).

hardwood native with a relatively stable canopy all year long, with only some minor increases in LAI in the summer (~1/2 LAI unit; Asner et al., 2006). This difference in LAI phenology spectrally translates itself in a higher NIR reflectance for *Morella* compared to *Metrosideros*. Similar to the trend in LAI the separability between the species NIR reflectances progressively increases towards the summer period, declining again in autumn and winter. This pattern was demonstrated when we recently analyzed the seasonal spectral properties of *Metrosideros* and *Morella* trees in the Hawaii Volcanoes National Park (in which our study area is located) using a four-year time series of Hyperion imagery (Somers & Asner, 2012). The linkage between ground phenology and satellite phenology is illustratively shown in Fig. 2.

The volcanic soils in the study area have little to no profile development and are very low in available N content (Vitousek et al., 1983). These low fertility soils explain the relatively low leaf N content of the native *Metrosideros* vegetation (0.7–0.9%). Due to its N-fixing capacity, the leaf N concentrations of *Morella* (1.5–1.9%; Asner et al., 2008b) are much higher. Consequently its litter systematically enriches soil fertility and in turn alters the ecosystem's nutrient balance (Vitousek & Walker, 1989; Vitousek et al., 1983). In addition, similar to most other invaders, *Morella* shows higher leaf chlorophyll (Chl-a for *Morella* 53 $\mu\text{g}/\text{cm}^2$ vs 40 $\mu\text{g}/\text{cm}^2$; Chl-b for *Morella* 20 $\mu\text{g}/\text{cm}^2$ vs 15 $\mu\text{g}/\text{cm}^2$ for *Metrosideros*) and carotenoid concentrations (18 $\mu\text{g}/\text{cm}^2$ and 12 $\mu\text{g}/\text{cm}^2$ for *Morella* and *Metrosideros* respectively), and consequently shows lower reflectance in the visible wavebands due to an increased photosynthetic capacity and light-use efficiency compared to *Metrosideros* (Asner et al., 2008b). During the winter, photosynthetic active radiation is low while rainfall is high. These unfavorable conditions cause a systematic yellowing of *Morella* foliage during the summer to winter transition period. In the winter–summer transition period, conditions change and leaf chlorophyll starts to build up again causing a progressive reduction in visible reflectance due to higher absorption of photosynthetic active radiation (Asner et al., 2006). Destructive field measurements show low leaf water (45–55% mass basis) concentrations for *Metrosideros* forests and moderate leaf water (50–65%) concentrations for the stands dominated by *Morella* in the study area (Asner & Vitousek, 2005). This is supported by lower NIR1 and SWIR reflectances for *Morella* compared to *Metrosideros*. During the hot summer conditions the differences in leaf water content, and consequently in NIR1 and SWIR reflectance, tend to minimize.

2.2. Field observations

For our study we had a set of 60 field observations of tree species locations (27 for *M. faya* and 33 for *M. polymorpha*; average uncertainty of ~2 m) acquired in January 2005. The validation samples were collected using a stratified random approach in which classes of mapped species were used to create the sampling strata. Within each stratum, a random point was selected using a random number generator for a grid based on the imagery (Asner & Vitousek, 2005). Each point indicates the presence of the species in the Hyperion image pixel.

2.3. Hyperion time series

For this study a time series of six cloud-free Hyperion image scenes covering our study area was available. We only used the images from August 2004 to July 2005 to coordinate classification results to the ground observations acquired in January 2005, i.e. all images fell within half a year of the field observations (Section 2.2). The EO-1 Hyperion sensor collects spectral information in 220 wavebands ranging from 400 to 2500 nm at a spatial resolution of 30 m (Pearlman et al., 2003). The images were acquired in August, September, October 2004 and January, March, July 2005 covering most of the major phenological events occurring within one year, i.e. flushing of *Morella* canopy in summer months (July, August, September), gradual yellowing of *Morella* leaves in the summer to winter transition period (October, January),

gradual build up of chlorophyll and expansion of *Morella* canopy in the summer–winter transition period (March) and the increased difference in canopy water content between both species in winter (January) (see Section 2.1; Fig. 2).

The time series data were geo-referenced and radiometrically processed at the Carnegie Institution for Science, Stanford, California. The ACORN-SLiBatch (ImSpec LLC, Palmdale, CA) atmospheric correction model (visibility = 50 km, water vapor retrieved using the 940 and 1140 nm absorption bands) was used to process each image to apparent surface reflectance. Subsequently, a destriping algorithm was applied to compensate for miscalibration between cross-track detectors. The down-track columns were summed, producing 256 values containing both a reflectance and calibration offset component; the reflectance was approximated by applying a Lee (1986) filter across the 256 values. Further, a cubic spline curve was fit to the 940 and 1140 nm water absorption bands to reduce the modeling effects introduced by atmospheric correction. Full details on the preprocessing can be found in Asner and Heidebrecht (2003). Due to its low signal to noise ratio (SNR) the 1800–2500 nm Hyperion wavebands were not considered in further analysis.

2.4. Multiple Endmember Spectral Mixture Analysis

Multiple Endmember Spectral Mixture Analysis (MESMA; Roberts et al., 1998) was used to translate each Hyperion reflectance image into sub-pixel cover fraction maps of *Metrosideros* and *Morella*. MESMA modeled a mixed spectrum as a combination of its constituent spectral components or spectral endmembers (i.e. native and invasive tree species in our case) weighted by their fractional cover in the pixel:

$$r = Mf + \varepsilon \quad \text{with} \quad \sum_{j=0}^m f_j \quad \text{and} \quad 0 \leq f_j \leq 1 \quad (1)$$

where \mathbf{M} is a $n \times m$ matrix of which each column corresponds to the spectral signal of a specific endmember or ground cover class and each row corresponds to a specific waveband. f is a column vector $[f_1, \dots, f_m]^T$ that denotes the sub-pixel cover fractions occupied by each of the m endmembers in the pixel. The portion of the spectrum that cannot be modeled is expressed as a residual term, ε . Sub-pixel endmember fractions were obtained by solving for the corresponding vector f such that ε_i^2 was minimized within the constraints of Eq. (1).

In MESMA the endmember matrix \mathbf{M} is allowed to vary on a per pixel basis to better model the inherent spectral variability within an image scene. In an iterative procedure, different endmember combinations, systematically selected from a spectral library, are used to decompose each pixel. The model with the best fit, i.e. with the lowest root mean square error (RMSE) in the reconstruction of the original pixel, is assigned to the pixel.

Species-specific spectral libraries for *Morella* and *Metrosideros* were required as input in MESMA. These were obtained from patches with approximately 100% *Morella* or *Metrosideros* cover as identified through a combination of field observations and an airborne, very high resolution image dataset (Asner & Vitousek, 2005). The Hyperion pixels that were located within these patches were selected to extract the species-specific spectral information from the Hyperion time series. For each species 25 pixels from five individual patches were extracted. Shadowing and shading effects were treated as an integral part of the spectral properties of each species and were therefore not included as a separate endmember in MESMA, as per the technique of Asner et al. (2008a).

2.5. Spectral feature selection for MESMA

2.5.1. Stable Zone Unmixing

To optimize the spectral separability between *Morella* and *Metrosideros*, we implemented the principles of Stable Zone Unmixing (SZU; Somers et al., 2010) into MESMA. This automated feature

extraction technique tries to maximize the spectral separability among endmembers by focusing the unmixing analysis on a subset of wavebands. First, the wavelengths' sensitivity to spectral separability between the endmember libraries (of *Morella* and *Metrosideros*; as described in Section 2.4) was evaluated using the Stability (or Separability) Index (SI), defined as the ratio of the inter-class and the intra-class variability:

$$SI_i = \frac{\Delta_{inter,i}}{\Delta_{intra,i}} = \frac{|R_{mean,1,i} - R_{mean,2,i}|}{1.96 \times (\sigma_{1,i} + \sigma_{2,i})} \quad (2)$$

where $R_{mean,1,i}$ and $R_{mean,2,i}$ are the mean reflectance values at wavelength i for endmember class 1 (e.g., *Metrosideros*) and endmember class 2 (e.g., *Morella*), respectively, whereas $\sigma_{1,i}$ and $\sigma_{2,i}$ are the standard deviations of classes 1 and 2, respectively. Higher SI values indicate better separability of the species in that specified waveband. By removing features from the analysis, however, spectral information is inevitably lost. Our aim was to obtain optimal cover fraction estimates and therefore a tradeoff was required between the number of spectral features included in the mixture analysis (i.e., – information) and the average SI of the considered features (i.e., – endmember variability/separability, noise).

The tradeoff protocol is summarized as follows: (i) the available wavebands are ordered according to its SI; (ii) the relative change in SI between successive (ordered) wavebands, d_{SI} , is evaluated against a tradeoff point. The tradeoff point, q , is the value of d_{SI} at which fraction estimate accuracy does not change when additional spectral features are removed from the mixture analysis. For $d_{SI} > q$ accuracy drops when additional features are removed, the opposite is true for $d_{SI} < q$. This inherently implies that the difference between q and d_{SI} (d_q) quantifies the amplitude by which fraction estimate accuracy increases/decreases by removing additional spectral features from the mixture analysis. In Somers et al. (2010) the tradeoff point was optimized for a set of simulated hyperspectral scenes covering natural, semi-natural and urban environments. For each scene the correct cover fraction distribution was known (since it were simulations) and in an iterative process the tradeoff point q resulting in the highest unmixing accuracy was determined. Results showed that for all scenes the optimal tradeoff q was 0.015 a value which was also adopted in this study; (iii) the accumulated d_q curve was calculated (D_{SI}) and the trend of this curve was shown to demonstrate a consistent resemblance with the MESMA accuracy. In previous work the robustness of the approach was demonstrated for a set of urban and natural environments under differing conditions (Somers et al., 2010). Consequently, D_{SI} modeled the trend in unmixing accuracy and its maximum indicated the number of wavebands needed for optimal cover fraction estimations.

2.5.2. Reducing spectral correlation in the selected subset

Here we propose an alternative SI-driven feature selection approach, referred to as uncorrelated SZU (uSZU), in which a boundary condition reduces the amount of correlation in the selected spectral subset. We hypothesize that redundant spectral information could be avoided and improved accuracy could be achieved with reduced computational time due to the selection of fewer bands in the mixture analysis.

Similar to SZU, uSZU starts with an analysis of the spectral libraries of *Metrosideros* and *Morella* (see Section 2.4). For each spectral band the SI value is calculated according to Eq. (2). The actual selection process, schematically overviewed in Fig. 3, then begins by selecting the waveband or spectral feature with the highest SI value. Subsequently, the spectral correlation (Corr) of the selected band (X) with all the other wavebands (Y) is calculated as the covariance (Cov) divided by the product of the standard deviations (σ) of the different wavebands:

$$corr(X, Y) = \frac{cov(X, Y)}{\sigma_X \sigma_Y} \quad (3)$$

Based on this spectral correlation matrix all bands that have a correlation with the selected waveband higher than a threshold c are discarded.

From the set of remaining wavebands (i.e., the selected band was not considered nor were the bands that were removed in the thresholding process), the band that now has the highest SI is selected as the second feature. Again, the bands that display a high correlation with this selected band are discarded from the remaining band set. However, the correlation threshold now decreases to $c-i$. This means that in this second run more wavebands are discarded from the analysis as all bands that now display a correlation with the selected band $> c-i$ (instead of $> c$ in the first run) are removed from the analysis. Subsequently, a third band is selected as the one with the highest SI in the remaining set and all remaining bands that display a correlation with that selected band $> (c-2 \times i)$ are removed from the analysis. This process continues until no more spectral features can be selected (or all bands are either selected for, or removed from, the analysis; Fig. 3).

Note that the correlation threshold progressively decreases with each newly selected band. The rationale for this is that we are seeking to balance the relation between the spectral separability (SI) and the spectral correlation in the final subset. With each run (or selection of a new band) the SI of the selected band decreases. The bands that are selected in the beginning of the process also display relatively high SI values. Yet, bands that are only selected after several runs most likely display much lower SI values, meaning that these bands had a significant overlap between the endmembers or tree species' reflectances and therefore are of low value in the unmixing process (Fig. 3). By progressively decreasing the correlation threshold we are also progressively increasing the number of bands that are removed from the analysis. In the beginning of the process the correlation threshold is high, resulting in only a few very highly correlated bands that are removed from the analysis. However, when the process continues, the maximum SI values decrease resulting in the selection of bands that display a lower separability (lower SI) but at the same time the number of wavebands that are removed from the remaining data set also drastically increases due to the decreased correlation threshold (Fig. 3). The decreasing threshold forces the selected subset to be composed of more bands with the highest discriminative power (highest SI), but possibly displaying a somewhat stronger inter-correlation. Consequently, fewer bands that are less correlated, but contain very similar spectral information between the endmembers (low SI), are included.

2.6. Multi-temporal MESMA

In an attempt to further reduce the spectral similarity among *Morella* and *Metrosideros* and improve the detection and map accuracy, we implemented a multi-temporal MESMA. An image cube was built composed of the spectral information of multiple Hyperion images and used as input into MESMA (Somers & Asner, in press). Similar temporal spectral composites were generated for the species specific endmember libraries (see Section 2.4). Subsequently, we applied the concepts of SZU and uSZU on these multi-temporal data providing subpixel estimates of *Morella* and *Metrosideros*.

In an operational setting, the available images are likely to change from year to year, because of variable weather conditions. The robustness of our multi-temporal MESMA was therefore evaluated using five different scenarios, drawing upon a different set of available images (and phenology). In the first scenario all six images of the time series were combined. As mentioned before, this set of images embeds different phenological differences between *Morella* and *Metrosideros*, i.e., flushing of *Morella* in summer, progressive yellowing of *Morella* leaves in winter, and chlorophyll built up in spring as well as increasing differences in water content concentrations between both species in winter. In the subsequent scenarios we used an iterative process of

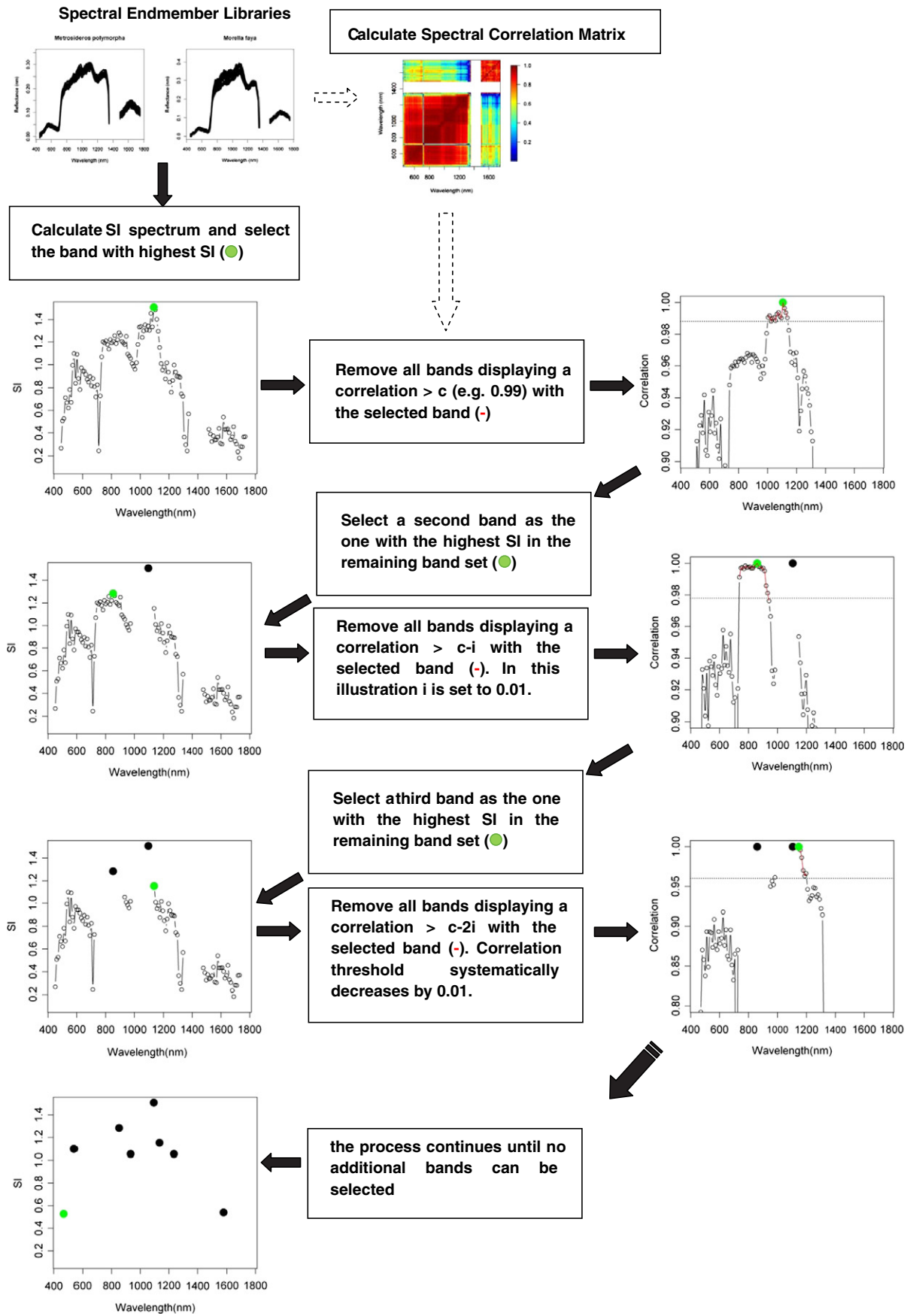


Fig. 3. Schematic overview of the uSZU band selection protocol.

systematically removing the image showing the highest detection success (the “best” image in terms of invasive species detection success) at each iteration. Fewer images inherently result in fewer phenological differences/events expressed in the spectral data.

2.7. Validation

The traditional MESMA, including all available spectral wavebands, and the SZU and the uSZU alternatives were applied to the Hyperion time series data. The unmixing techniques were applied on all images individually (unitemporal approach) as well as on the multi-temporal scenarios described in Section 2.6. The relative performance of the different MESMA approaches was assessed through a soft to hard classification conversion as per the technique of Somers and Asner (in press). The sub-pixel cover maps of *Morella* provided by MESMA were cross-referenced to the field observations of known tree positions described in Section 2.2. All sub-pixel cover fraction values exceeding a predefined threshold were assigned to *Morella*, all fraction values below this threshold were assigned to *Metrosideros*. All possible thresholds (between 1 and 100% in steps of 1%) were iteratively evaluated in order to identify the optimal threshold.

3. Results

3.1. Unitemporal MESMA

In this section we focus on the unitemporal implementation of MESMA, i.e. applied on a single image. The traditional MESMA analysis, including all available 117 wavebands, revealed a seasonal trend in the detection success of *Morella*, as shown in Fig. 4. Highest Kappa coefficients were observed in summer and winter months while a clear drop in accuracy occurred in March and October. The higher accuracy for July and August can be explained by the difference in NIR reflectance due to intensive leaf flushing in *Morella*. The higher detection accuracy in winter can be explained by both the yellowing of *Morella* leaves and the increase in leaf water content differences between *Morella* and *Metrosideros*. Both phenological events express themselves by differences in the visible and SWIR reflectance domains respectively. Optimal Kappa values for the summer period (July–October) were obtained for a MESMA threshold around 25% (i.e., in the hard classification, all cover fraction values exceeding this threshold were assigned to *Morella*, all fraction values below this threshold were assigned to *Metrosideros*),

while a shift towards 45% was observed for March and January. In the remainder of the text we only reported on the optimal Kappa coefficients, in order to allow a transparent evaluation of the different unmixing techniques.

The SZU analysis, for which results are summarized in Table 1, reinforces our hypothesis that a SI-based waveband selection improves *Morella* detection. For all six images, an increase in Kappa was observed (Table 1). Also, after band selection between 63 (August) and 105 (October) spectral bands were used in the MESMA analysis (Table 1). An additional benefit of the SZU was that the computational time was approximately 10 to 50% shorter compared to the traditional analysis including all of the original 117 wavebands.

The adaptive character of SZU is clearly demonstrated in Fig. 5, showing for each image the selected wavebands and corresponding SI values. For each image, SZU selected a different set of wavebands corresponding to the spectral dynamics of *Morella* and *Metrosideros*. The waveband selection process was inherently driven by plant phenology. This can be illustrated by focusing on the SWIR reflectance. As mentioned in Section 2.1, the foliar water concentrations of *Morella* and *Metrosideros* differed slightly in winter but were almost identical in summer, resulting in similar SWIR reflectance. Our separability (SI) analysis nicely mirrored this phenological event by showing SI values for the SWIR reflectance of 0.6 in January–March, and 0.4 in August–July (Fig. 5). Driven by these relative differences in SI, SZU automatically discarded the SWIR reflectance in summer while retained this information in winter, improving the invasive species detection success in both cases.

Notwithstanding these promising results, it is clear that the spectral subsets selected by SZU still contain many highly correlated adjacent and therefore possibly redundant wavebands (Fig. 5). We therefore anticipated that further improvements in classification accuracy (and computing time) were feasible and we applied an adapted SI driven waveband selection procedure reducing the overall correlation within the spectral subset (see 2.5.2). The optimal Kappa coefficients for this new uSZU_{*i*} approach, at different levels of *i* (i.e. the iterative factor by which the correlation threshold decreased, see 2.4.2), are shown in Table 1.

In general, uSZU_{*i*} systematically improved the detection success of *Morella* compared to the traditional MESMA including all original 117 wavebands (Table 1). The exception is January, which for uSZU_{0.005} (*i* = 0.005) showed a drop in Kappa from 0.66 to 0.60. Furthermore, the number of selected wavebands was drastically reduced to 32 to

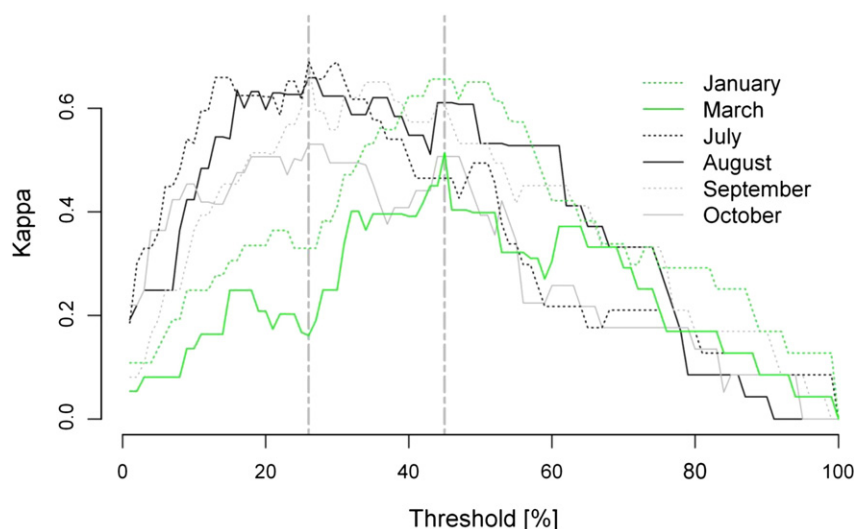


Fig. 4. The seasonal trends in the success of detecting *Morella* invasion, expressed as the Kappa coefficient, as a function of the MESMA classification threshold, are shown for each month. The vertical dotted lines indicate the maximum Kappa values for thresholds of 45% (obtained in January/March) and 25% (obtained in July/August/September/October; adapted from Somers & Asner, in press).

Table 1

The seasonal trends in the success of detecting *Morella* invasion, expressed as the Kappa coefficient, for the different unmixing approaches. The number of bands used in the analysis (n°) are also indicated. Kappa results are shown for the optimal or maximal Kappa. In between parentheses the MESMA classification threshold at which the highest Kappa was achieved is given.

	MESMA		SZU		uSZU _{0.001}		uSZU _{0.005}		uSZU _{0.01}		SZU _{0.005}		uSZU _{fixed}	
	Kappa	n°	Kappa	n°	Kappa	n°	Kappa	n°	Kappa	n°	Kappa	n°	Kappa	n°
January	0.66 (46)	117	0.66 (49)	86	0.73 (42)	36	0.60 (46)	23	0.70 (45)	15	0.60 (43)	23	0.60 (39)	35
March	0.51 (45)	117	0.56 (45)	88	0.53 (48)	41	0.59 (45)	19	0.54 (42)	13	0.55 (46)	19	0.52 (48)	30
July	0.69 (38)	117	0.73 (30)	74	0.72 (33)	32	0.73 (31)	15	0.71 (39)	10	0.65 (34)	15	0.65 (38)	12
August	0.66 (30)	117	0.70 (20)	63	0.73 (29)	34	0.73 (23)	12	0.73 (26)	9	0.69 (24)	12	0.72 (23)	14
September	0.69 (31)	117	0.73 (28)	90	0.67 (28)	45	0.75 (23)	21	0.72 (31)	14	0.69 (26)	21	0.69 (31)	27
October	0.53 (52)	117	0.61 (52)	105	0.62 (41)	32	0.69 (31)	13	0.66 (34)	8	0.60 (36)	13	0.62 (40)	11

45 bands for uSZU_{0.001}, 12 to 23 bands for uSZU_{0.005}, and 8 to 15 bands for uSZU_{0.01}, resulting in an average gain in computational time compared to the traditional MESMA of respectively 65%, 70% and 85%.

The spectral subsets selected by uSZU_{0.005} are shown in Fig. 5. The number of highly correlated adjacent wavebands was greatly reduced while critical phenological events were better highlighted. In August most of the selected bands are from the NIR plateau. This makes sense since the intensive flushing of *Morella* is the major phenological event in this month causing a significant difference in NIR reflectance. In September and October, conditions for *Morella* start to become suboptimal causing yellowing of its canopy. This reflects itself in a more significant contribution of visible wavebands in the uSZU selected subsets.

Compared to SZU we observed a slight increase in invasive species detection success, except for March ($i = 0.001$) and July ($i = 0.01$) where a small drop in Kappa was observed (Table 1). The reduction in computational time compared to SZU was on average 40%, 65% and 75% for uSZU_{0.001}, uSZU_{0.005} and uSZU_{0.01}, respectively. In order to further justify the selection of decorrelated wavebands, we compared our results to the ones obtained by a SZU approach, referred to as SZU_{0.005}, in which the same number of wavebands were selected as in uSZU_{0.005}, however, spectral correlation was not taken into account (i.e., only the wavebands with the highest SI values were selected irrespective of their level of inter-correlation). Kappa coefficients were systematically lower compared to the traditional SZU as well as uSZU_{0.005}, which nicely confirmed our hypothesis (Table 1). Some of the critical phenological events are masked by only selecting the wavebands with the highest SI. For instance, in January the 23 bands displaying the highest SI values are all visible bands. This is due to the yellowing of *Morella* leaves. However, differences in leaf water content between *Morella* and *Metrosideros* are also most expressed in winter. While SZU_{0.005} only selects 23 visible bands, SZU and uSZU account for the difference in leaf water content by, in addition to visible bands, also including SWIR reflectance bands in their analysis. Thereby they better modeled the differences in plant phenology which on its turn improves the detection success.

The correlation parameter i , used to steer the waveband selection process in uSZU _{i} (see 2.4.2.), obviously had an influence on the type and number of selected wavebands and the invasive species detection success (Table 1). The best accuracies were generally obtained for uSZU_{0.005}. For uSZU_{0.01} (i.e., $i = 0.01$) the selected subsets became relatively small and notwithstanding a 33% improvement in run time, the *Morella* detection success was generally reduced compared to uSZU_{0.005}. Recall that uSZU _{i} started with the selection of the waveband with the highest SI, while all remaining wavebands that were strongly correlated to this selected band were removed from the analysis. In a second run, a new band (highest SI) was selected and again all wavebands that were highly correlated to this band were removed from analysis. This procedure continued until no bands were left to select or remove (see Fig. 3). With each run (or selection of a new band), the correlation tradeoff or threshold decreased, indicating that once the first band was selected, the correlation threshold for uSZU_{0.001} became $1-0.001$ (i.e., i) = 0.999. For uSZU_{0.01} the

threshold was $1-0.01 = 0.990$. So while in uSZU_{0.001} all bands with a correlation >0.999 were removed from the analysis, uSZU_{0.01} removed all bands with a correlation >0.990 . After selection of the second waveband, the threshold for uSZU_{0.001} was reduced to $0.999-0.001 = 0.998$ while for uSZU_{0.01} all wavebands that had a correlation with the selected band higher than $0.990-0.01 = 0.980$ were removed from the analysis. Results showed that for uSZU_{0.01} the band selection process was severe and too many wavebands were removed at the expense of relevant information (Fig. 6). This contrasts the result for uSZU_{0.001}, in which the remaining subset size was too big, i.e. too many correlated wavebands were present, also resulting in a drop in Kappa compared to uSZU_{0.005} (Table 1).

As illustrated above, the key aspect of our uSZU _{i} band selection approach is the correlation threshold, which systematically increased each time a new waveband was added to the subset. The removal of correlated bands became more progressed/severe with decreasing SI. This was needed to balance the relation between the spectral separability (SI) and the spectral correlation in the final subset. By progressively decreasing the correlation threshold we could exclude the wavebands that showed the highest overlap in reflectance between our tree species (lowest SI) in the analysis. This is illustrated in Fig. 6, which shows the difference between the subsets selected by uSZU_{0.01} and those selected with a fixed correlation threshold of 0.96, i.e. uSZU_{fixed}. In this case, more bands were retained and the retained bands on average had a lower SI, resulting in a decrease in the invasive species detection success, as illustrated in Table 1. By using a fixed threshold some of the critical phenological events are masked from the spectral subset; e.g. as mentioned before the NIR bands are the most distinctive bands in July, August as they mirror the flush in *Morella*. Yet, when a fixed correlation threshold is used, the contribution of these NIR bands in the final subset is minor as most of the selected bands now come from the blue reflectance which shows a relatively low SI value and does not reflect any known important phenological event (Fig. 6).

3.2. Multi-temporal MESMA

Thus far, our analysis has focused on the application of MESMA on individual images (unitemporal MESMA). Yet previous work already demonstrated the benefits of combining spectral information of different periods in the growing season (or different images) to detect *M. faya* infestations in the native *Metrosideros* forests of our study area (Somers & Asner, in press). When all six images of the times series were combined in a single data cube (i.e., $117 \times 6 = 702$ spectral bands) and implemented in MESMA, a Kappa of 0.73 was obtained (Table 2), compared to 0.69, the maximum Kappa that could be obtained with the unitemporal MESMA approach. It should be mentioned that this improvement for multi-temporal MESMA came at the expense of a significant increase in running time. With 702 bands to be processed, the multi-temporal approach was about 80% slower than the unitemporal approach, in which only 117 spectral bands were used.

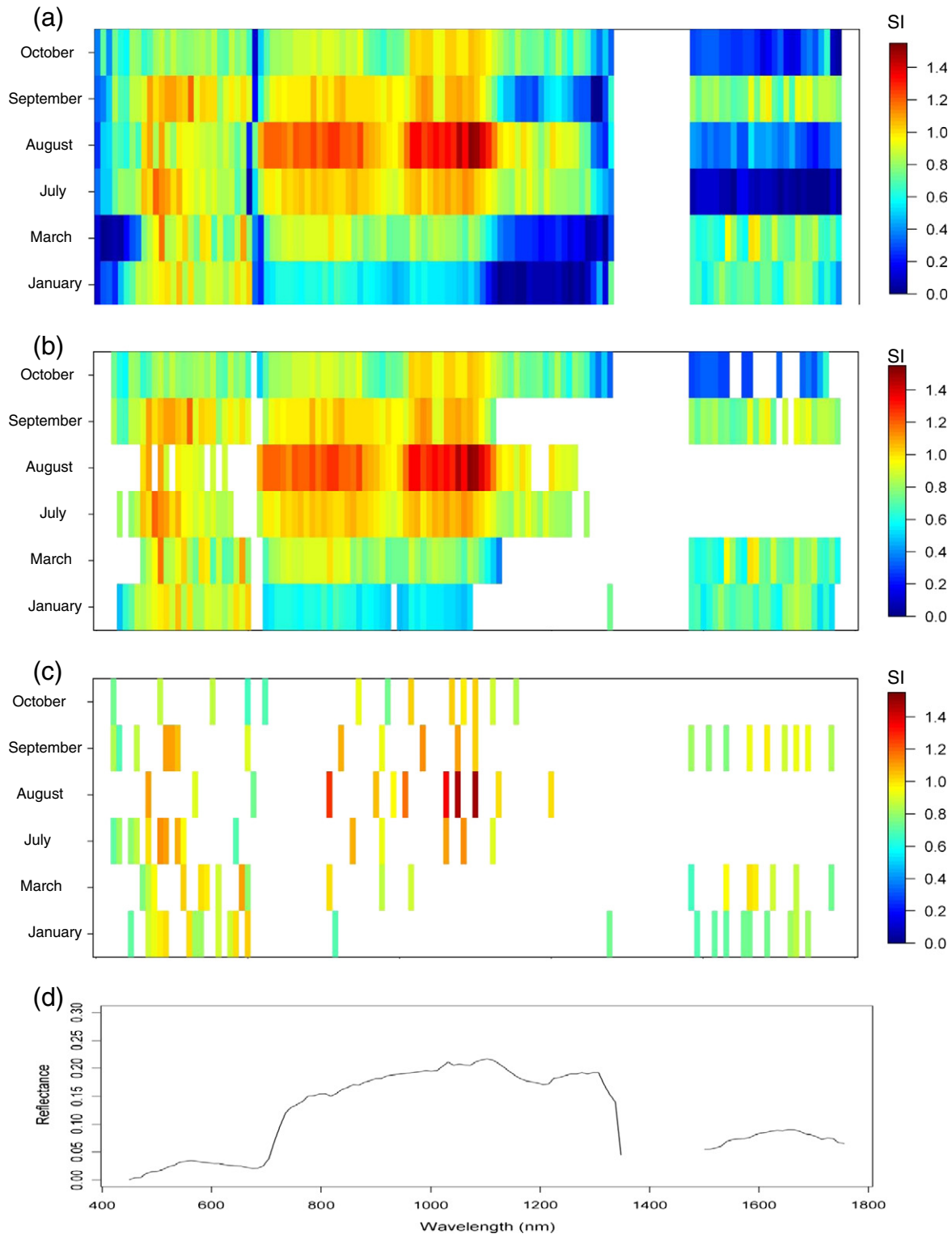


Fig. 5. Spectro-temporal SI charts for the unitemporal implementation of (a) traditional MESMA including all 117 bands per image, (b) SZU and (c) uSZU_{0.005}. Panel (d) shows a random vegetation spectrum. The X and Y axis of the different SI charts represent the spectral bands and the time scale respectively.

The temporal analysis allowed us to capture plant phenology. As opposed to the unitemporal analysis, spectral unmixing was now able to optimize the spectral difference between *Metrosideros* and *Morella* by simultaneously accounting for the summer flushing of *Morella* (NIR in August), the yellowing of *Morella* leaves in the summer to winter transition period (VIS in September–January) and the increased difference in canopy water content in winter (SWIR in January).

Yet our experimental results demonstrate that a multi-temporal MESMA did not always result in better *Morella* detection (Table 2). To simulate the fact that the set of available images can change from year to year, because of variable weather conditions, we tested the multi-temporal MESMA for five different scenarios, drawing upon a different set of available images. Starting from all six available images, in each subsequent scenario the image showing the highest detection success

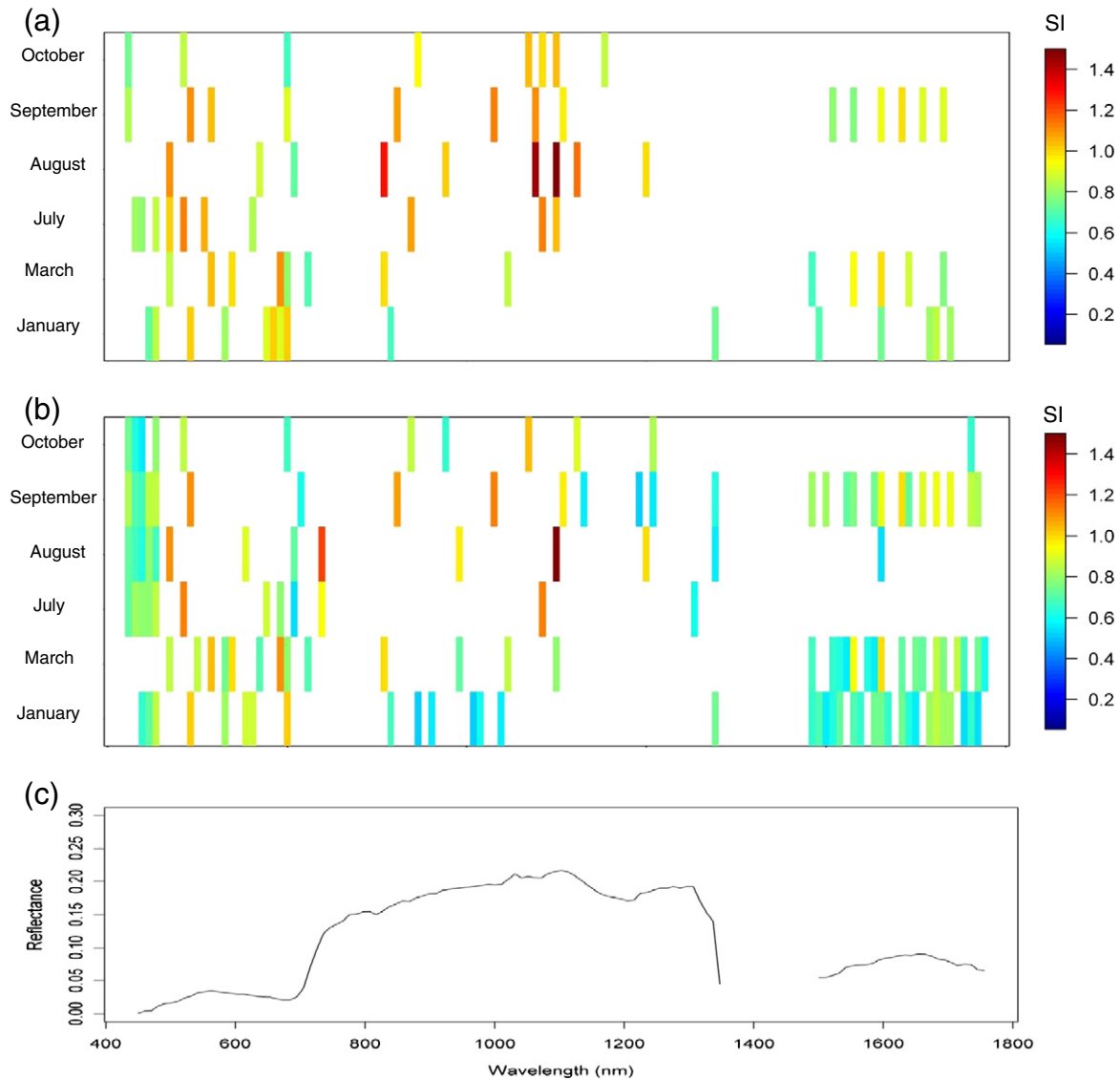


Fig. 6. Spectro-temporal SI charts for the unitemporal implementation of (a) $uSZU_{0.01}$ and (b) $uSZU_{fixed}$. The latter is the $uSZU$ algorithm in which the correlation threshold is fixed to 0.96. This as opposed to a progressively decreasing threshold in $uSZU$. Panel (d) shows a random vegetation spectrum. The X and Y axis of the different SI charts represent the spectral bands and the time scale respectively.

in the unitemporal analysis (Table 1) was removed. While the first scenario (scenario I, Table 2) contained the spectral information of all six images (and thus embedded all major phenological events), the last scenario (scenario V, Table 2) only incorporated the spectra of March and October, i.e., the two months showing the lowest detection success in the unitemporal approach (Table 1, Section 3.1). Analysis showed that for scenarios I–III the multi-temporal analysis was effective

(Table 2). However, for scenarios IV & V this was not the case as here the spectral composing showed a significant reduction in the detection success of *Morella* (Table 2). This can be explained by the fact that in March and October the subtle differences in phenology between *Metrosideros* and *Morella* are moderate and constrained to some visible (start of chlorophyll built up in *Morella*) and SWIR (start of depletion of water content in *Morella*) bands in March and visible (start of chlorosis

Table 2

The success of detecting *Morella* invasion, expressed as the Kappa coefficient, through multi-temporal unmixing. Results are shown for different scenarios drawing upon a different set of available images and for the different unmixing algorithms. The number of bands used in the analysis (n°) are also indicated. Kappa results are shown for the optimal or maximal Kappa. In between parentheses the MESMA classification threshold at which the highest Kappa was achieved is given.

Scenario		MESMA		SZU		$uSZU_{0.001}$		$uSZU_{0.005}$		$uSZU_{0.01}$		$SZU_{0.005}$		$uSZU_{fixed}$	
		Kappa	n°	Kappa	n°	Kappa	n°	Kappa	n°	Kappa	n°	Kappa	n°	Kappa	n°
I	Jan, Mar, Jul, Aug, Sep, Oct	0.73 (34)	702	0.73 (35)	544	0.76 (36)	105	0.75 (28)	36	0.78 (26)	23	0.74 (29)	37	0.69 (23)	37
II	Jan, Mar, Aug, Sep, Oct	0.72 (36)	585	0.76 (39)	458	0.74 (44)	96	0.75 (25)	35	0.78 (26)	22	0.73 (21)	35	0.72 (25)	35
III	Jan, Mar, Aug, Oct	0.72 (39)	468	0.72 (37)	354	0.73 (31)	82	0.75 (22)	34	0.78 (39)	21	0.73 (21)	34	0.73 (22)	34
IV	Jan, Mar, Oct	0.54 (51)	351	0.54 (43)	262	0.56 (38)	80	0.75 (44)	31	0.66 (46)	19	0.53 (39)	31	0.53 (44)	31
V	Mar, Oct	0.40 (51)	234	0.48 (50)	172	0.58 (46)	58	0.59 (41)	25	0.60 (46)	15	0.53 (39)	25	0.48 (47)	27

in *Morella*) and NIR (differences in LAI) bands in October (Fig. 7). Consequently, most of the bands in the temporal composite of March and October are bands that show a low SI or a significant spectral overlap between both species (i.e. ‘overlapping bands’) while only a few bands show some distinct differences (i.e. ‘information bands’). The multi-temporal unmixing solution will be biased towards the overwhelming

amount of ‘overlapping bands’ compared to ‘information bands’ resulting in a drop in detection success.

When the concepts of SZU were implemented in multi-temporal MESMA, we generally observed a consistent increase in Kappa (Table 2). The selected subsets remained fairly large, i.e. ~75% of the original dataset. Consequently, compared to the full multi-temporal

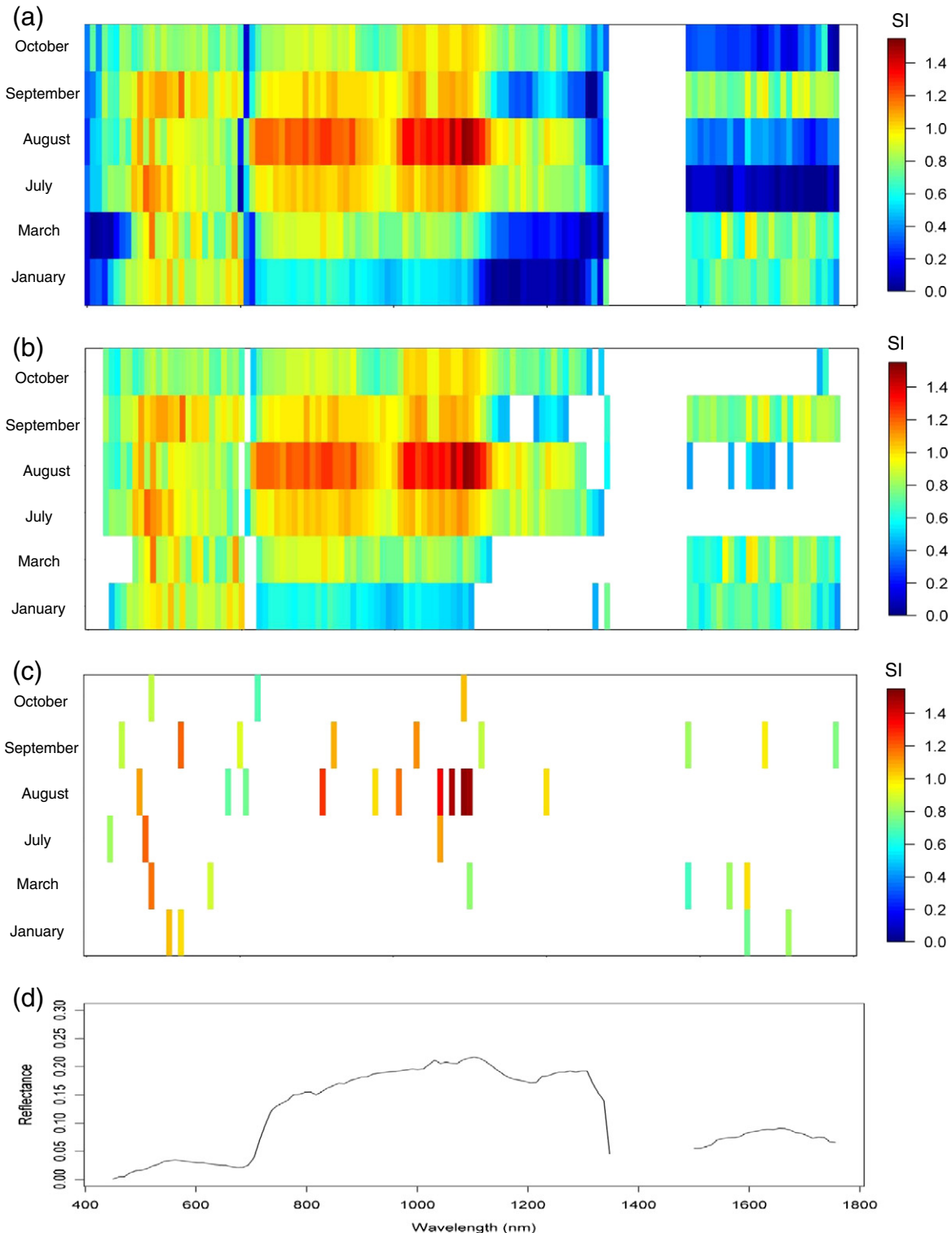


Fig. 7. Spectro-temporal SI charts for the multi-temporal implementation of (a) MESMA, (b) SZU and (c) uSZU_{0.005}. Panel (d) shows a random vegetation spectrum. The X and Y axes of the different SI charts represent the spectral bands and the time scale respectively.

approach the average reduction in computational time was only ~25% (Fig. 7; Table 2).

However, by removing the correlated bands in the selected subset through uSZU, the size of the selected subsets was dramatically decreased to 15–25% for uSZU_{0.001}, 5–11% for uSZU_{0.005}, 3–7% for uSZU_{0.01}, resulting in a run time that was decreased by ~80%, 90% and 95% respectively (Fig. 7). However, even more importantly, we also noticed an increase in the detection success of *Morella* compared to the traditional MESMA and SZU (except for scenario II where only an increase in accuracy compared to SZU was observed when i was increased to 0.01 (uSZU_{0.01} in Table 2)). The general increase in detection success can be explained by the fact that, similar to the unitemporal approach, the selected subset better highlights the phenological differences between *Metrosideros* and *Morella*. In other words, it masks the “overlapping bands”. This is illustrated in Fig. 7. In general, one can state that from January, March and July green reflectance bands are selected as a result of the progressive chlorophyll buildup of the *Morella* leaves in response to the progressively more intense photosynthetic active radiation in the winter to summer transition period. In September, October and January, the opposite occurs, in which red reflectance bands are selected as a consequence of the yellowing of *Morella* due to unfavorable winter conditions. The effect of leaf flushing in *Morella* is included in the analysis by the selection of NIR bands from July, August and September, while the higher leaf water content for *Morella* in winter expresses itself in the selection of SWIR bands from January and March. For Scenario V (results not shown) this implies that the uSZU only selected some green and SWIR bands in March and some red and NIR bands in October, corresponding to the subtle phenological differences between *Metrosideros* and *Morella* observed in these times of year. All “overlapping bands” were now removed from the temporal composite resulting in a significant higher detection success for the March–October temporal composite ($Kappa = 0.60$, Table 2) compared to the unitemporal results of both months ($Kappa_{March} = 0.51$, $Kappa_{October} = 0.53$).

Overall, higher Kappa's were observed for uSZU_{0.01}, SZU_{0.005}, i.e. SZU using the same number of selected bands as was used in uSZU_{0.005}, also provided relatively good results, yet still not as good as its uSZU equivalent (Table 2). Also the use of a fixed correlation coefficient (i.e. 0.96, uSZU_{fixed}) did not match the accuracy of the uSZU approach this again due to the selection of more ‘unstable’ (lower SI) wavebands (Table 2) and the masking of critical phenological events.

4. Discussion & conclusions

Applying SZU on individual images (unitemporal approach, Section 3.1) resulted in a systematic increase of the invasive species detection success compared to traditional MESMA (Table 1), which corroborates the results of Somers et al. (2010). However, in contrast to previous studies, we were now able to verify the benefits of SZU when applied in an actual mapping/detection context using satellite imagery. The study of Somers et al. (2010) only tested the approach using simulated image data compiled from in situ measured reflectance spectra but never verified the true potential of the approach on actual remote sensing data. The benefits of SZU were threefold. By carefully selecting wavebands that optimized the separability between the considered endmembers, we not only achieved a higher detection accuracy, but we could further reduce the computational time by 10 to 50% (Table 1). In contrast to AutoSWIR (Asner & Lobell, 2000), SZU had the additional advantage of being able to automatically adapt to the considered scenario or image scene. While in each image of the time series AutoSWIR is focused on the SWIR2 reflectance, the SZU selected subsets that automatically changed throughout the year (Fig. 5b). Band selection was guided by the spectral separability among the endmembers present, which in our vegetation monitoring context was strongly driven by the phenological differences among the target plant species.

The benefits of SZU were much less expressed in the multi-temporal MESMA analysis though (Table 2). When the spectral information of different images was combined, the SI driven band selection selected too many bands, i.e. ~75% of the available band set (Table 2; Fig. 7). In SZU band selection is driven by the relative change in SI between consecutive wavebands (when ordered according to decreasing SI, i.e. d_{SI} , see 2.5.1). In short, as long as the decrease in SI between consecutive bands was small, no bands were removed from the analysis. Only when the difference in SI increased drastically, were bands removed. This is illustrated in Fig. 8, showing the average decrease in SI for the unitemporal images and the temporal composite containing the spectral information of all six images. The average number of wavebands selected by SZU in the unitemporal approach was 84 which corresponded to the clear drop in the unitemporal SI profile (Fig. 8b). The multi-temporal SI profile, on the other hand, declined much slower such that as many as 544 bands were retained in the unmixing analysis resulting in only a slight increase in Kappa (and decrease in computational time) compared to the multi-temporal MESMA model including all 702 wavebands. The increased correlation that often occurs between similar spectral wavebands at different moments of the year (Somers & Asner, 2012) might explain the relatively high number of bands retained in the multi-temporal SZU. This implies that the multi-temporal SZU selects too many “overlapping bands” (i.e. bands in which the spectral properties of *Metrosideros* and *Morella* strongly overlap) and fails to properly highlight the crucial phenological events that allow optimization of the spectral differences between both species (Fig. 7).

By reducing the correlation in the selected subsets through uSZU we overcame this problem. The size of the selected subsets, and consequently the computational time of the unmixing process, was drastically reduced while a more effective detection of *Morella* was achieved. This occurred for both the unitemporal and the multi-temporal approach (Tables 1 & 2; Figs. 5c and 7c). The approach nicely highlights the crucial phenological differences between *Morella* and *Metrosideros*, e.g. summer flushing in *Morella* canopies (NIR in August), progressive yellowing of *Morella* leaves in the summer to winter transition period (VIS in September), and the increased difference in canopy water content in winter (SWIR in January). Compared to the traditional MESMA and SZU approaches the multi-temporal uSZU results were less dependent on the available spectral information (i.e. the different scenarios). This was especially true for uSZU_{0.005}. The optimal Kappa of 0.75 was achieved for scenario I, containing the spectral information of all six images (and thereby embeds most of the major phenological events), but also for scenario IV in which only the spectral information of January, March and October was available (Table 2). Recall that January, March and October, were the months showing the lowest Kappa in the unitemporal approach (Table 1). Although, spectral differences between *Morella* and *Metrosideros* in March and October were present, they were mainly constrained to a few narrow waveband zones. Consequently, most of the bands in the March and October images were bands that showed a significant spectral overlap between both species while only a few bands showed some relevant differences. It was expected that without further band selection the temporal composite of January, March and October would not result in a high *Morella* detection success, as shown in Table 2. However, by carefully masking the “overlapping”, and highlighting the “discriminative” bands the subtle phenological differences between *Morella* and *Metrosideros* were highlighted, resulting in an improvement of the detection success. This is an important observation because this stresses the fact that despite the lack of imagery covering all phenological events, a proper band selection strategy emphasizing the subtle spectral and phenological differences between species can partly compensate for this lack of data. This opens perspectives for mapping efforts in areas where cloud cover is a limiting factor for building extended spectral image time series.

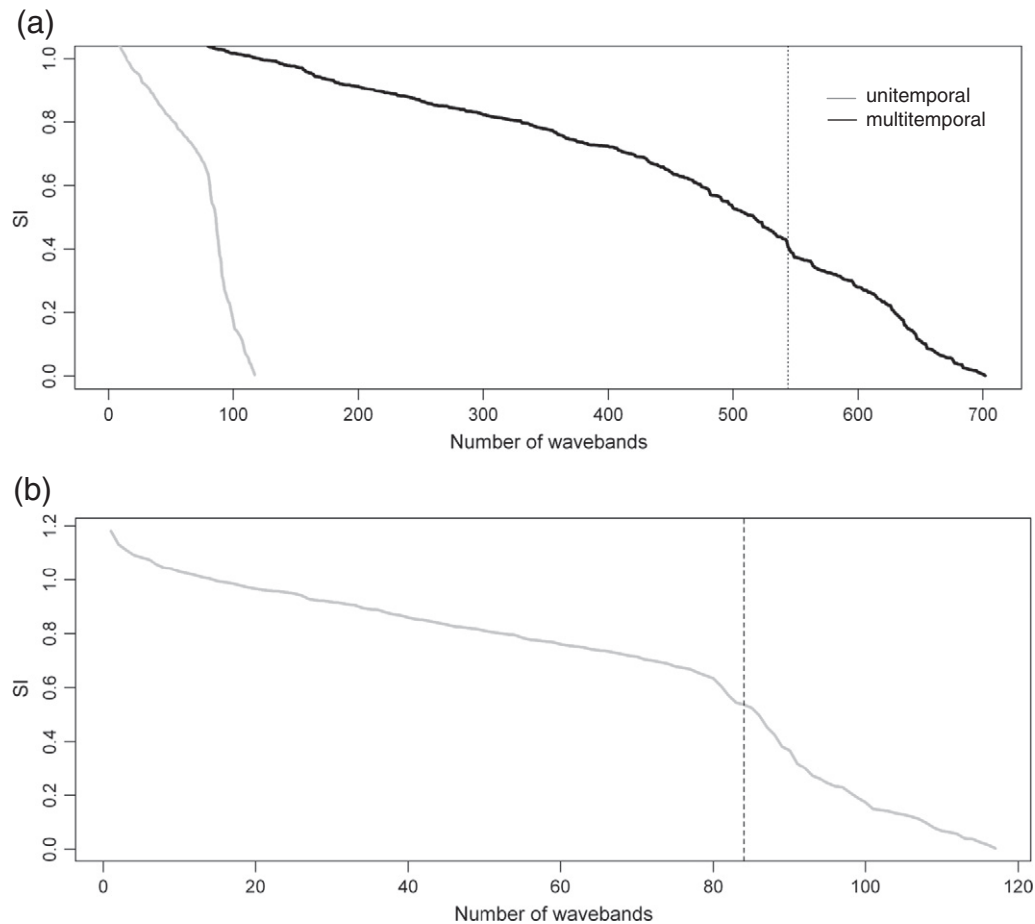


Fig. 8. The band selection protocol of SZU is driven by the relative change in SI between consecutive wavebands (when ordered according to decreasing SI, i.e. d_{SI} , 2.4.1.). In (a) the average decrease in SI for all individual images (unitemporal) with increasing band numbers is compared to the decrease in SI for the temporal composite, containing the spectral information of all six available bands (multitemporal). Due to the gradual decrease in SI as much as 544 wavebands (indicated by the vertical dotted line) were selected by multi-temporal SZU. In the unitemporal approach, for which a detail is shown in (b), 84 bands were selected corresponding to the clear drop in the SI profile (indicated by the vertical dotted line).

Overall, we demonstrated the benefits of multi-temporal hyperspectral unmixing, but also showed that a proper feature selection strategy is required to emphasize plant phenology and fully optimizing the invasive species detection success. These conclusions extend and strengthen the findings of Somers et al. (2011), showing that an integration of different conceptual approaches (i.e., iterative mixture cycles, feature selection, temporal analysis) is needed to optimally address endmember variability issues in spectral mixture analysis. Despite the promising results, we acknowledge that further research is still required to optimize uSZU. Currently, we are evaluating an approach to expand uSZU to more complex forest scenes with a mosaic of species. Relying on the iterative mixture analysis principles of MESMA, we are exploring a modified unmixing strategy in which each pixel is evaluated using different spectral subsets, each tuned towards maximal separability of a specific endmember class combination or species mixture. A SI class matrix is therefore evaluated according to the uSZU principles. Instead of using the same spectral subset to unmix each image pixel, our modified approach would allow the spectral subsets to vary on a per pixel basis such that each pixel is evaluated using a spectral subset tuned towards maximal separability of its specific endmember class combination or species mixture, and this according to the feature selection principles presented in uSZU. Second, although our results generally showed an increase in accuracy compared to traditional MESMA and SZU, uSZU was highly sensitive to the correlation threshold parameter i (see 2.5.2; Tables 1 & 2; Figs. 5 & 6). While the most accurate results for the unitemporal

approach were obtained for $i = 0.005$, highest accuracies for the multi-temporal approach were obtained for $i = 0.01$. Further research should not only verify the robustness of uSZU in other regions or ecosystems but also the relationship between i and the uSZU output requires additional investigation.

Although the concepts of multi-temporal classification and the combined feature selection approach are in this study specifically calibrated for spectral unmixing, other pixel-based classification techniques for tropical forest mapping (e.g., Cochrane, 2000; Heumann, 2011; Papes et al., 2010; Thenkabail et al., 2004) can benefit from the presented concepts.

Acknowledgments

The authors thank three anonymous reviewers for their comments and suggestions, which greatly helped to improve the scientific content and presentation of the manuscript. The research presented in this paper is funded by the Belgian Science Policy Office in the framework of the STEREO II Programme - Project VEGEMIX (SR/67/146). The Carnegie Airborne Observatory is made possible by the Gordon and Betty Moore Foundation, the John D. and Catherine T. MacArthur Foundation, W. M. Keck Foundation, the Margaret A. Cargill Foundation, Grantham Foundation for the Protection of the Environment, Avatar Alliance Foundation, Mary Anne Nyburg Baker and G. Leonard Baker Jr., and William R. Hearst III. This study was supported by a grant from the NASA Terrestrial Ecology Program and the National

Science Foundation grant DEB-0715593. The scientific input of Roberta Martin, David Knapp, Laurent Tits, Reinout Van Bets, and Kristof Van Tricht is gratefully acknowledged.

References

- Armstrong, R. W. (1983). *Atlas of Hawaii* (2nd ed.). State of Hawaii, Honolulu: University of Hawaii Press.
- Asner, G. P., & Heidebrecht, K. B. (2003). Imaging spectroscopy for desertification studies: Comparing AVIRIS and EO-1 Hyperion in Argentina drylands. *IEEE Transactions on Geoscience and Remote Sensing*, 41, 1283–1296.
- Asner, G. P., Knapp, D. E., Kennedy-Bowdoin, T., Jones, M. O., Martin, R. E., Boardman, J., et al. (2008a). Invasive species detection in Hawaiian rainforests using airborne imaging spectroscopy and LIDAR. *Remote Sensing of Environment*, 112, 1942–1955.
- Asner, G. P., Knapp, D. E., Kennedy-Bowdoin, T., Jones, M. O., Martin, R. E., Boardman, J., et al. (2008b). Remote sensing of native and invasive species in Hawaiian rainforests. *Remote Sensing of Environment*, 112, 1912–1926.
- Asner, G. P., & Lobell, D. B. (2000). A biogeophysical approach for automated SWIR unmixing of soils and vegetation. *Remote Sensing of Environment*, 74, 99–112.
- Asner, G. P., Martin, R. E., Carlson, K. M., Rascher, U., & Vitousek, P. M. (2006). Vegetation–climate interactions among native and invasive species in Hawaiian rainforest. *Ecosystems*, 9, 1041–1054.
- Asner, G. P., & Vitousek, P. M. (2005). Remote analysis of biological invasion and biogeochemical change. *Proceedings of the National Academy of Sciences of the United States of America*, 102, 4383–4386.
- Asner, G. P., Wessmann, C. A., Bateson, C. A., & Privette, J. L. (2000). Impact of tissue, canopy, and landscape factors on the hyperspectral reflectance variability of arid ecosystems. *Remote Sensing of Environment*, 74, 69–84.
- Clark, M., Roberts, D. A., & Clark, D. B. (2005). Hyperspectral discrimination of tropical rain forest tree species at leaf to crown scales. *Remote Sensing of Environment*, 96, 375–398.
- Cochrane, M. A. (2000). Using vegetation reflectance variability for species level classification of hyperspectral data. *International Journal of Remote Sensing*, 21, 2075–2087.
- Daughtry, C. S. T. (2001). Discriminating crop residues from soil by shortwave infrared reflectance. *Agronomy Journal*, 93, 125–131.
- Delalieux, S., van Aardt, J. A. N., Keulemans, W., Schrevens, E., & Coppin, P. (2007). Detection of biotic stress (*Venturia inaequalis*) in apple trees using hyperspectral data: non-parametric statistical approaches and physiological implications. *European Journal of Agronomy*, 27, 130–143.
- Dennison, P. E., & Roberts, D. A. (2003). The effects of vegetation phenology on endmember selection and species mapping in Southern California Chaparral. *Remote Sensing of Environment*, 87, 123–135.
- Giambelluca, T. M., Nullet, M. A., & Schroeder, T. A. (1986). *Rainfall atlas of Hawaii*. State of Hawaii, Honolulu: Department of Land and Natural Resources.
- Glenn, N. F., Mundt, J. T., Weber, K. T., Prather, T. S., Lass, L. W., & Pettingill, J. (2005). Repeat hyperspectral data processing for the detection of small infestations of leafy spurge. *Remote Sensing of Environment*, 95, 399–412.
- Hall, S., & Asner, G. P. (2007). Biological invasion alters regional N-oxide emissions from tropical rainforests. *Global Change Biology*, 13, 2143–2160.
- He, K. S., Rocchini, D., Neteler, M., & Nagendra, H. (2011). Benefits of hyperspectral remote sensing for tracking plant invasions. *Diversity and Distributions*, 17, 381–392.
- Hesketh, M., & Sanchez-Azofeifa, G. A. (2012). The effect of seasonal spectral variation on species classification in the Panamanian Tropical Forest. *Remote Sensing of Environment*, 118, 73–82.
- Hestir, E. L., Khanna, S., Andrew, M. E., Santos, M. J., Viers, J. H., Greenberg, J. A., et al. (2008). Identification of invasive vegetation using hyperspectral remote sensing in the California Delta ecosystem. *Remote Sensing of Environment*, 112, 4034–4047.
- Heumann, B. W. (2011). Satellite remote sensing of mangrove forests: recent advances and future opportunities. *Progress in Physical Geography*, 35, 87–108.
- Huang, C., & Asner, G. P. (2009). Applications of remote sensing to alien invasive plant studies. *Sensors*, 9, 4869–4889.
- Lawrence, R. L., Wood, S. D., & Sheley, R. L. (2006). Mapping invasive plants using hyperspectral imagery and Breiman Cutler classifications (RandomForest). *Remote Sensing of Environment*, 100, 356–362.
- Lee, J. S. (1986). Speckle suppression and analysis for synthetic aperture radar images. *Optical Engineering*, 25, 636–643.
- Li, J. (2004). Wavelet-based feature extraction for improved endmember abundance estimation in linear unmixing of hyperspectral signals. *IEEE Transactions on Geoscience and Remote Sensing*, 42, 644–649.
- Miao, X., Gong, P., Swope, S., Pu, R., Carruthers, R., Anderson, G. L., et al. (2006). Estimation of yellow starthistle abundance through CASI-2 hyperspectral imagery using linear spectral mixture models. *Remote Sensing of Environment*, 101, 329–341.
- Papes, M., Tupayachi, R., Martinez, P., Peterson, A. T., & Powell, G. V. N. (2010). Using hyperspectral satellite imagery for regional inventories: a test with tropical emergent trees in the Amazon Basin. *Journal of Vegetation Science*, 21, 342–354.
- Parker, W. A. E., & Hunt, E. R. (2004). Accuracy assessment for detection of leafy spurge with hyperspectral imagery. *Journal of Range Management*, 57, 106–112.
- Pearlman, J. S., Barry, P. S., Segal, C. C., Shepanski, J., Beiso, D., & Carman, S. L. (2003). Hyperion, a space-based imaging spectrometer. *IEEE Transactions on Geoscience and Remote Sensing*, 41, 1160–1173.
- Richardson, A. D., Duigan, S. P., & Berlyn, G. P. (2002). An evaluation of noninvasive methods to estimate foliar chlorophyll content. *New Phytologist*, 153, 185–194.
- Roberts, D. A., Gardner, M., Church, R., Ustin, S., Scheer, G., & Green, R. O. (1998). Mapping Chaparral in the Santa Monica mountains using multiple endmember spectral mixture models. *Remote Sensing of Environment*, 65, 267–279.
- Roberts, D. A., Smith, M. O., & Adams, J. B. (1993). Green vegetation, nonphotosynthetic vegetation, and soils in AVIRIS data. *Remote Sensing of Environment*, 44, 255–269.
- Somers, B., & Asner, G. P. (in press). Invasive species mapping in Hawaiian rainforests using multi-temporal Hyperion spaceborne imaging spectroscopy. *IEEE Journal of Selected Topics in Applied Earth Observations and Remote Sensing*, <http://dx.doi.org/10.1109/JSTARS.2012.2203796> (in press).
- Somers, B., & Asner, G. P. (2012). Hyperspectral time series analysis of native and invasive species in Hawaiian rainforests. *Remote Sensing*, 4, 2510–2529.
- Somers, B., Asner, G. P., Tits, L., & Coppin, P. (2011). Endmember variability in spectral mixture analysis: A review. *Remote Sensing of Environment*, 115, 1603–1616.
- Somers, B., Delalieux, S., Verstraeten, W. W., van Aardt, J. A. N., Albrigo, G., & Coppin, P. (2010). An automated waveband selection technique for optimized hyperspectral mixture analysis. *International Journal of Remote Sensing*, 31, 5549–5568.
- Thenkabail, P. S., Enclona, E. A., Ashton, M. S., Legg, C., & De Dieu, M. J. (2004). Hyperion, IKONOS, ALI, and ETM plus sensors in the study of African rainforests. *Remote Sensing of Environment*, 90, 23–43.
- Underwood, E., Ustin, S., & DiPietro, D. (2003). Mapping nonnative plants using hyperspectral imagery. *Remote Sensing of Environment*, 86, 150–161.
- Vitousek, P. M., Mooney, H. A., Lubchenco, J., & Melillo, J. M. (1997). Human domination of Earth's ecosystems. *Science*, 277, 494–499.
- Vitousek, P. M., Van Cleve, K., Balakrishnan, N., & Mueller-Dombois, D. (1983). Soil development and nitrogen turnover in montane rainforest soils in Hawaii. *Biotropica*, 15, 268–274.
- Vitousek, P. M., & Walker, L. R. (1989). Biological invasion by *Myrica faya* in Hawaii: Plant demography, nitrogen fixation, ecosystem effects. *Ecological Monographs*, 59, 247–265.
- Vitousek, P. M., Walker, L. R., Whiteacre, L. D., Mueller-Dombois, D., & Matson, P. A. (1987). Biological invasion by *Myrica faya* alters ecosystem development in Hawaii. *Science*, 238, 802–804.
- Whiteaker, L. D., & Gardner, D. E. (1992). Fire tree (*Myrica faya*) distribution in Hawaii. Honolulu, HI: University of Hawaii Coop. Nat. Park Res. Studies Unit.
- Zhang, J., Rivard, B., Sanchez-Azofeifa, A., & Castro-Esau, K. (2006). Intra- and inter-class spectral variability of tropical tree species at La Selva, Costa Rica: Implications for species identification using HYDICE imagery. *Remote Sensing of Environment*, 105, 129–141.